RESEARCH ARTICLE

Dominant Role of Hole Transport Pathway in Achieving Record High Photoconductivity in Two-Dimensional Metal-Organic Frameworks

Denan Wang,[a‡] Sarah Ostresh,[b‡] Daniel Streater,[c] Peilei He,[c] James Nyakuchena,[c] Qiushi Ma,[a] Xiaoyi Zhang,[d] Jens Neu,[e*] Gary W. Brudvig,[b*] and Jier Huang[a,c*]

[a] Prof. J. Huang, Dr. D. Wang, Q. Ma
Department of Chemistry, Schiller Institute for Integrated Science and Society, Boston College,
Chestnut Hill, Massachusetts 02467, United States
E-mail: jier.huang@bc.edu

[b] Prof. G. Brudvig, Dr. S. Ostresh
Department of Chemistry and Yale Energy Science Institute, Yale University,
New Haven, Connecticut, 06520-8107, United States
E-mail: gary.brudvig@yale.edu

[c] Prof. J. Huang, Dr. D. Wang, D. Streater, Dr. P. He, J. Nyakuchena
Department of Chemistry, Marquette University
Milwaukee, WI, 53201, United States

[d] Dr. X. Zhang
X-ray Science Division, Argonne National Laboratory,
Argonne, Illinois, 60349, United States

[e] Prof. J. Neu
Department of Physics, University of North Texas,
Denton, Texas, 76205 United States
E-mail: jens.neu@unt.edu

Supporting information for this article is given via a link at the end of the document.

Abstract: Metal-organic frameworks (MOFs) with mobile charges have attracted significant attention due to their potential applications in photoelectric devices, chemical resistance sensors, and catalysis. However, fundamental understanding of the charge transport pathway within the framework and the key properties that determine the performance of conductive MOFs in photoelectric devices remain underexplored. Herein, we report the mechanisms of photoinduced charge transport and electron dynamics in the conductive 2D M-HHTP (M=Cu, Zn or Cu/Zn mixed; HHTP=2,3,6,7,10,11-hexahydroxytriphenylene) MOFs and their correlation with photoconductivity using the combination of time-resolved terahertz spectroscopy, optical transient absorption spectroscopy, X-ray transient absorption spectroscopy, and density functional theory (DFT) calculations. We identify the through-space hole transport mechanism through the interlayer sheet π-π interaction, where photoinduced hole state resides in HHTP ligand and electronic state is localized at the metal center. Moreover, the photoconductivity of the Cu-HHTP MOF is found to be 65.5 S•m^{-1}, which represents the record high photoconductivity for porous MOF materials based on catecholate ligands.

Introduction

Metal-organic frameworks (MOFs), a novel class of porous crystalline materials built from metal nodes coordinated by bridging organic linkers, have emerged as next generation functional materials for diverse applications including gas storage and separation, catalysis, sensors, and drug delivery.[1] However, the use of MOFs as semiconducting charge transport materials in photoelectronic devices is relatively limited due to their inherently poor electrical conductivity.[2] Benefiting from the abundance of building blocks and structural diversity, recent progress in developing 2D MOFs have resulted in the discovery of conductive MOFs, where the conductivity can transport either through-bond via metal-to-ligand/ligand-to-metal charge transfer or through-space by processes that include π-π interactions between sheets and charge-hopping.[3] These 2D conducting or semiconducting MOFs have further extended the applications of MOFs to supercapacitors,[4] charge storage materials,[5] thermoelectric devices,[6] chemical resistance sensors,[7] electrochemical catalysis,[8] as well as photocatalysis.[9] For example, recent studies by Castaldelli and coworkers reported a naphthalene diimide-based MOF, which demonstrates electrochemical activity, electrical semi-conductivity, and photoactivity, which was attributed to its conductive nature that facilitates charge delocalization.[10] As another example, Pattengale et al. reported a conductive MOF based on Zn_2TTFTB (TTFTB=tetrathiafulvalene tetrabenzoate), which not only exhibits light absorption and photoconductivity, but also undergoes ultrafast charge separation through electron transfer to a TiO_2

photoanode owing to facile hole migration from the interfacial region.[11]

Despite these findings, few studies provide fundamental insights on the correlation of MOF structure with the photoconductivity mechanism; yet they are essential to further develop conductive MOFs for photoelectronics and photocatalytic applications.[3j-l] In this work, we report the photoinduced hole transport in Cu-HHTP MOFs ($Cu_3(HHTP)_2$; HHTP=2,3,6,7,10,11-hexahydroxytriphenylene) as well as the correlation of the carrier dynamics with the MOF structure and photoconductivity. Using the combination of optical pump THz probe (OPTP), optical transient absorption (OTA) spectroscopy, and X-ray transient absorption (XTA) spectroscopy, supported by density functional theory (DFT) calculations, we unambiguously uncover that the photoinduced hole transport occurs through interlayer π-π interaction between HHTP ligands, which is primarily responsible for the photoconductivity in Cu-HHTP. Notably, the photoconductivity of Cu-HHTP sets a new benchmark for porous MOF materials using catecholate ligands, reaching an impressive value of 65.5 S/m.

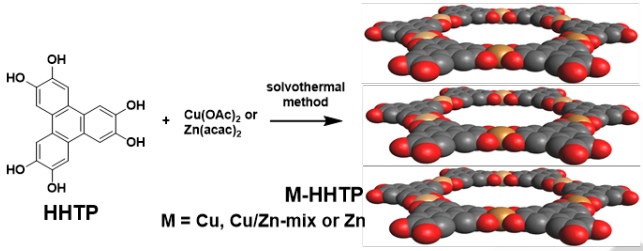

Scheme 1. Synthetic scheme and structure illustration of stacking mode of 2D-MOF M-HHTP (M = Cu, Cu/Zn or Zn).

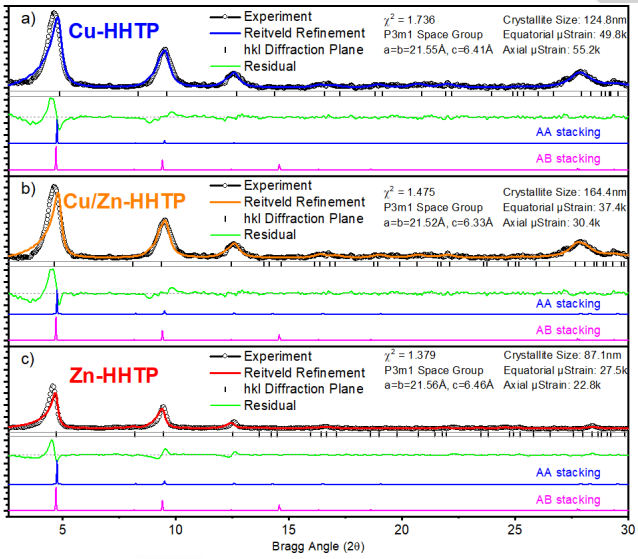

Figure 1. Experimental and simulation of PXRD pattern of a) Cu-HHTP; b) Cu/Zn-HHTP; c) Zn-HHTP (black cycle: experimental data; solid line: Rietveld refinement).

Results and Discussion

M-HHTP MOFs (M = Cu, Cu/Zn or Zn) are synthesized following the established synthetic protocols (Scheme 1) with minor modification.[12] Zn-HHTP and mixed node Cu/Zn-HHTP MOFs are synthesized to unravel the impact of redox inactive metal nodes on charge transport mechanism and photoconductivity (Zn has a $3d^{10}$ electron configuration). The atomic ratio of Cu to Zn in Cu/Zn-HHTP is ~ 64:36, as indicated by energy dispersive X-ray spectroscopy (EDX) (Figure S1). The crystallinity of M-HHTP is evaluated by powder X-ray diffraction (PXRD). As shown in Figure 1, the PXRD patterns of Zn-HHTP and Cu/Zn-HHTP show good agreement with the peaks characteristic of Cu-HHTP,[7f] suggesting that all three MOF samples have similar topology and crystallinity. The approximate stacking orientation of the 2D layers is obtained by simulating diffraction patterns in VESTA for AA and AB packing models with 2D sheets aligned along the c-axis. In comparison to AB, the AA stacking orientation simulation matches better with the experimental data. Diffraction 2θ peaks located near 4.7°, 9.5°, and 12.6° are common between both AA and AB, but the AB model predicts a prominent peak near 14.5° 2θ that is not observed in the PXRD pattern. Nonetheless, the PXRD patterns indicate good crystallinity and long-range order in the ab plane, while the diffraction peak at 27.9° in the simulated pattern is assigned to the (002) diffraction plane, which confirms that the ab plane is stacked along the c axis with about 3.2 Å as the interlayer distance in all three MOFs. Furthermore, the instrument parameters of the Rigaku Miniflex II used to obtain the PXRD patterns were found by fitting to a SiO_2 standard which allows for the crystalline size and strain that are responsible for diffraction peak broadening of M-HHTP MOFs to be obtained by Rietveld refinement. While crystallite size does not follow any apparent trend, which is further supported by scanning electron microscope (SEM) measurements (Figure S1), crystallite strain appears to increase with the concentration of Cu, suggesting Cu plays a role causing disorder within the MOF microcrystals.

The formation of M-HHTP MOFs is further evaluated by Fourier-transform infrared (FTIR) spectroscopy. As shown in Figure 2a, the broad OH stretch at ~3300 cm^{-1} observed in the spectrum of the free ligand vanishes after the metalation reaction. This is accompanied by the formation of a new band at 1649 cm^{-1} in the spectra of all three M-HHTP MOFs, which can be assigned to C=O stretch and suggests that the ligands have been partially oxidized during the reaction. In addition, the two bands at 1475 cm^{-1} and 1420 cm^{-1} can be attributed to C=C stretches, which are associated with the ligand aromatic ring. These results together suggest the successful formation of the MOF structure by the assembly of metal ions and HHTP ligands. The FTIR spectra of all three M-HHTP MOFs show similar patterns, which supports the analogous structures of these MOFs, consistent with the XRD results discussed above. The diffuse reflectance UV-visible spectra of Cu-HHTP, Zn/Cu-HHTP, and Zn-HHTP show two prominent absorption bands at 350−420 nm and 480−720 nm and additional absorption in the NIR region (Figure 2b). As the UV-visible absorption spectrum of HHTP (Figure S2) has distinct features (centered at 275 nm) from those of the M-MOFs, we attributed these broad features to the conjugation in 2D MOFs. Note that these absorption features are also observed in Zn-HHTP MOF which has Zn^{2+} with $3d^{10}$ electron configuration,

although the latter shows a slightly narrower spectrum beyond 600 nm, suggesting that these absorption bands are mainly associated with the ligand centered transitions.

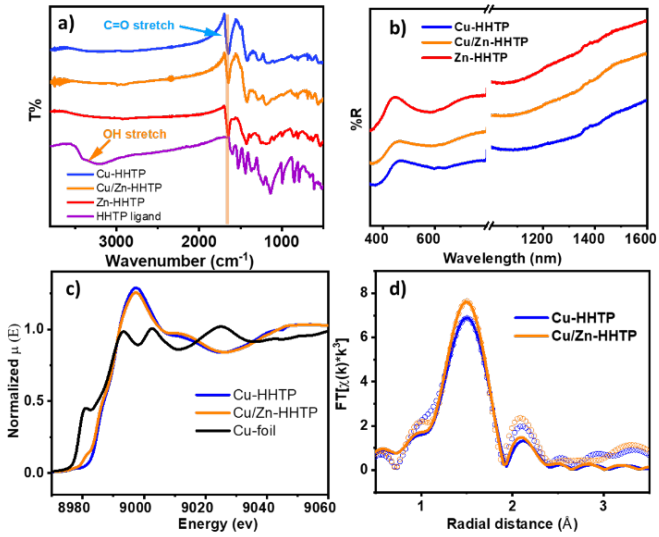

Figure 2. a) FTIR spectra of 2D M-HHTP MOFs and HHTP ligand (offset is used for clarity); b) diffuse reflectance UV-Visible spectra of Cu-HHTP, Zn/Cu-HHTP, and Zn-HHTP (offset is used for clarity); c) XANES spectra of Cu-HHTP, Zn/Cu-HHTP, and Cu-foil at Cu K-edge; d) The Cu-edge Fourier-transformed EXAFS spectra of Cu-HHTP and Cu/Zn-HHTP in R-space. Open circles and solid lines are experimental and FEFF fitting results, respectively.

In addition to the bulk structure, the local structure at Cu centers in Cu-HHTP and Cu/Zn-HHTP is examined using steady-state X-ray absorption spectroscopy (XAS). As shown in Figure 2c, the X-ray absorption near edge structure (XANES) spectra of Cu-HHTP and Cu/Zn-HHTP measured at the Cu K-edge show two prominent absorption features at 8.982 and 8.998 keV, which can be attributed to 1s→ $4p_z$ (+shakedown) and 1s→$4p_{xy}$, respectively, and result from the ligand of the square planar Cu center having less impact in the z-direction, lowering the energy of the 1s-$4p_z$ transition.[3l] Note that the XANES spectrum of the Cu center in the Zn/Cu-HHTP MOF resembles that of Cu-HHTP, suggesting that the incorporation of Zn has negligible effect on the local structure of the Cu center in the Cu/Zn-HHTP MOF, which is consistent with PXRD and FTIR results. This is further supported by quantitative analysis of their extended X-ray absorption fine structure (EXAFS) spectra (Figures 2d and S3). As shown in Figure 2d and Table S1, quantitative analysis on these EXAFS data yields a Cu-O distance of ~1.94-1.95 Å with each Cu coordinated by four O for both Cu-HHTP and Zn/Cu-HHTP, suggesting that the Cu centers in both samples have a similar local environment, i.e. square planar geometry at the Cu center. Moreover, the XANES spectrum of Cu/Zn-HHTP at the Zn K-edge resembles that of Zn-HHTP (Figure S4), which is featured by the prominent 1s-4p transition at 9.666 keV, suggesting a similar coordination geometry at the Zn center for both MOFs. The quantitative analysis of EXAFS spectra results in a Zn-O distance of 1.99 Å (Figure S4 and Table S1) for both MOFs, where each Zn center is coordinated by four O atoms, suggesting that Zn replaced Cu in Cu/Zn-HHTP.

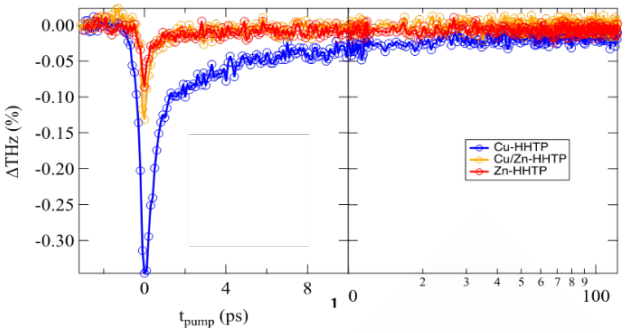

Figure 3. OPTP traces of Cu-HHPT, Cu/Zn-HHTP, and Zn-HHTP MOFs using tape cells. The solid lines are used to guide the eyes. Cu-HHTP exhibits the largest photoconductivity of the three, attenuating the THz signal by 0.3%. At the vertical cutline the y-axis changes from linear to logarithmic.

Optical pump terahertz probe (OPTP) spectroscopy was used to compare the photoconductivity between Cu-HHTP, Cu/Zn-HHTP and Zn-HHTP MOFs (Figure 3). OPTP is a non-contact technique to measure the photoconductivity, as THz radiation is readily absorbed by mobile carriers. A 400 nm pulse photoexcites the sample and THz pulses probe the sample following photoexcitation with an adjustable femtosecond time delay, spanning 125 ps. Changes in the THz peak amplitude correspond to photoinduced free carriers. The pump power was 90 mW and the samples were thick enough to absorb the pump pulse completely. Cu-HHTP exhibits a photoconductive THz attenuation of 0.3%, significantly larger than the previously reported photoconductivity of other MOFs.[11a] The addition of Zn to the MOF structure strongly diminishes this signal. OPTP spectroscopy probes the excited state properties of a material, in particular its picosecond time scale photoconductivity. The ground state of the material (without excitation) is measured using THz Time Domain Spectroscopy (TDS). THz-TDS was used to determine the absorption coefficient, refractive index, and permittivity of Cu-HHTP at three temperatures: 300 K, 200 K, and 100 K (Figure S5). Conductivity is the product of the mobile charge density and the mobility of these charges. The mobility of charge carriers in a band is expected to increase upon cooling, contrary to the observed trend. However, the density of thermally activated charge carriers is expected to decrease upon cooling. This effect is referred to as freezing out of charge carriers. The absorption coefficient, refractive index, and permittivity all appear to shift lower with temperature, suggesting that free charges are frozen out and the material is semiconductive, in agreement with the reported photoconductivity.[13] It is remarkable that the overall photoconductivity of Cu-HHTP (65.5 $S \cdot m^{-1}$) (details in SI) is six times higher than previously reported ground-state conductivity results (10 $S \cdot m^{-1}$),[13] and the best point of reference currently available for spectroscopic photoconductivity results of catecholate type MOFs (Table S3).

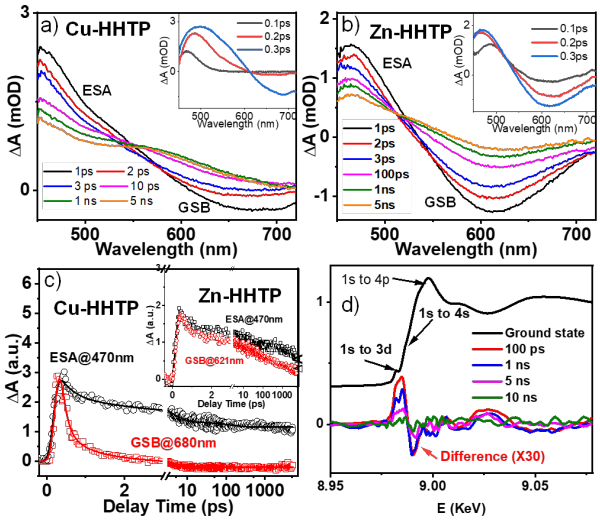

Figure 4. OTA spectra of a) Cu-HHTP and b) Zn-HHTP with 400 nm excitation. c) The comparison of the GSB and ESA kinetics of Cu-HHTP and Zn-HHTP (inset); d) XANES spectrum of Cu-HHTP and the difference XANES spectra at Cu K-edge. The difference spectra were obtained by subtracting the laser-off spectrum from the laser-on spectrum (100 ps, 1 ns, 5 ns, and 10 ns) for Cu-HHTP.

To gain insight into the nature of charge transport in M-HHTP MOFs, we examined their excited state dynamics using optical transient absorption (OTA) spectroscopy. As shown in Figure 4a, the early time OTA spectra of Cu-HHTP (< 0.3 ps) mainly consists of a negative band centered at ~680 nm and a positive band at ~550 nm with an isosbestic point at 610 nm. The ~680 nm negative feature is consistent with the peak in the steady-state absorption spectrum and can thus be assigned to the ground state bleach (GSB) band where electrons are moved from the valence band to some higher energy, previously unoccupied band thereby reducing the absorption at those wavelengths. The positive feature can be attributed to the excited state absorption (ESA) of the electron that was moved into the higher energy band. It is interesting to note that the isosbestic point between the GSB and ESA moves from 610 nm to 570 nm at early time (< 3 ps) and further moves to 560 nm at later time (> 100 ps), suggesting that the system relaxes to form a new intermediate state (IMS). A similar spectral evolution was observed in the OTA spectra of Cu/Zn-HHTP (Figure S6) and Zn-HHTP (Figure 4b), suggesting that a similar IMS is observed in all three samples. On the other hand, compared to Cu-HHTP, the isosbestic points at a similar time regime for the different samples becomes more and more blue shifted while the GSB becomes narrower with an increasing concentration of Zn in M-HHTP MOFs. These results are consistent with literature results on a zirconium-based MOF (NU-1000)[14] and our previous findings on M-THQ MOFs,[3l] which can be attributed to the decreasing delocalization of carriers and carrier density in M-HHTP MOFs when Cu^{2+} is increasingly replaced by Zn^{2+}. Accordingly, the formation of the IMS during ESA relaxation is likely associated with the carrier trapping. This assignment is further supported by a comparison of the ESA decay and the GSB recovery kinetics, where recovery of the GSB is more rapid than the ESA decay in all three samples (Figure 4c and S6). In addition, the difference between the GSB recovery and the ESA decay becomes smaller in the Zn-HHTP sample (Figure 4c). This can be explained by the relaxation of electrons from the conduction band to a more localized state and holes being filled by electrons to form a more energetically favored state, which gives rise to the faster recovery of the GSB than the ESA.

The kinetic traces of M-HHTP were fitted using a multi-exponential decay function and the fitting parameters are listed in Table S2. The time constant for exciton relaxation from the delocalized state to a localized state is ultrafast (~0.2-1 ps) in Cu-HHTP and Cu/Zn-HHTP, after which it forms a long-lived excited state (>> 5 ns). In Zn-HHTP, the initial relaxation occurs in ~1-1.2 ps, which is followed by a long-lived excited state (> 5 ns). The slower early time relaxation kinetics in Zn-HHTP than that of Cu-HHTP and Cu/Zn-HHTP can be explained by the inert Zn center in Zn-HHTP that blocks the trapping of carriers through a ligand-to-metal charge transfer (LMCT) pathway and instead relaxation of the photoelectron proceeds only through HHTP localized states, which is confirmed later by XTA.

The nature of the long-lived component was evaluated using XTA, which allows us to directly probe the electron density at the Cu center in Cu-HHTP. Figure 4d shows the XANES spectrum of Cu-HHTP at the Cu K-edge, which features a strong white line absorption corresponding to the Cu 1s−4p transition. Also shown in Figure 4d are the difference spectra obtained after subtracting the ground state XANES spectrum from the spectrum collected at delay times at 100 ps, 1 ns, 5 ns, and 10 ns following 400 nm excitation, which demonstrates the transient signals of Cu. A clear positive feature was observed at 8.99 keV, which overlaps with the 1s−4p transition edge, indicating that the edge energy of Cu shifts to lower energy. This suggests that photoexcitation of Cu-HHTP leads to the reduction of Cu center in Cu-HHTP, i.e. the photoexcited intermediate species has LMCT nature. This LMCT state decays as the intensity of the difference spectra collected at delay times at 1 ns, 5 ns, and 10 ns decreases with time. This is further supported by the kinetics studies, where the intensity of the difference signal at 8.99 eV decays with time (Figure S7). However, the kinetic trace only decays 70% at 80 ns, indicating that there is a very long lifetime component that correlates with the long-lived component we observed in OTA spectra, i. e. the long-lived species is likely a more localized state with LMCT nature.

To better understand the origins of exceptional photoconductivity and carrier dynamics in Cu-HHTP, density functional theory (DFT) under the planewave approximation was employed using VASP 6.2.1. The structure optimization and band structure calculations are detailed in the supporting information (Figure S8-S10). Band structure calculations can help to understand energy levels and electronic localization, and serve to provide a ground state picture of the electronic structure. Our calculations use the screened hybrid functional HSE06, which improves on the commonly used generalized gradient approximation (GGA) functionals like PBE that tend to overestimate delocalization and underestimate band gaps. Results from these calculations indicate that Cu-HHTP has a minimum band gap along the ML k-line of 0.07 eV, a band gap of 0.08 eV along KH, 0.13 eV along ALHA, and 0.49 eV along GMKG (Figure 5). Notably, GMKG is the only k-line in which the

valence band does not cross the Fermi level implying Cu-HHTP has semi-metallic behavior. Common features of the band structure along the various k-lines are a series of bands ~0.5–1.0 eV, ~2.5 eV and ~3.0–4.0 eV above the Fermi level which are attributed by the atom projected density of states to belong predominantly to HHTP, Cu, and HHTP, respectively. The main benefit of utilizing the screened hybrid HSE06 functional is that it allows for a more accurate representation of band energies than what would be obtained by the pure GGA PBE functional. This allows us to assert that since the excitation wavelength used in the included photophysical studies is 400 nm (3.1 eV) the HHTP band ~3.0 eV above the Fermi level is likely populated initially after excitation before filling unoccupied Cu^{2+} orbitals in Cu-HHTP. The resulting long-lived photoelectron is not conductive as the Cu bands are flat; however, the left-behind hole will contribute to the photoconductivity according to dispersive valence bands.

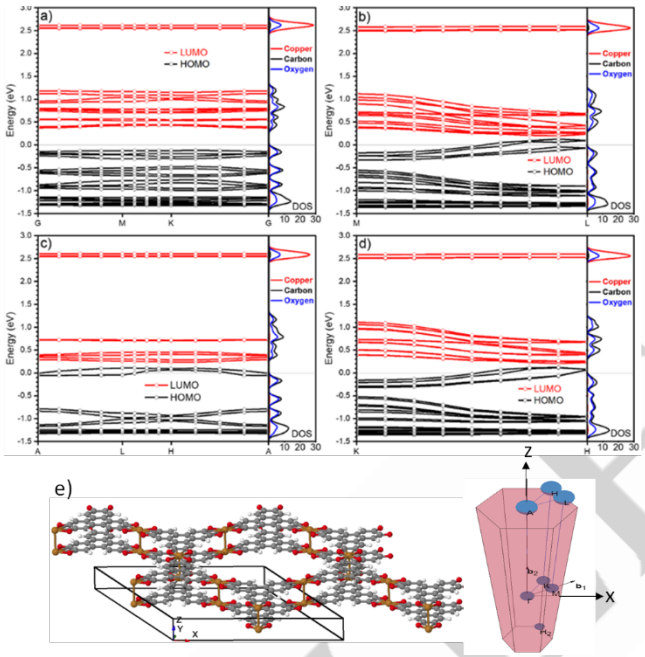

Figure 5. Band structure of Cu-HHTP along (a) G-M-K-G k-lines, (b) M-K k-line, (c) A-L-H-A k-lines (d) K-H k-line and (e) the illustration of two-layer Cu-HHTP MOF structure and projection of path.

Although the DFT calculations cannot directly predict system dynamics after photoexcitation, the larger dispersion of the valence bands on the ML and KH k-lines indicate that they are likely responsible for hole mobility, allowing us to infer that this mobility is observed in the OPTP experiment. The flat Cu band 2.5 eV above the fermi level is spatially isolated and energetically isolated from the C and O dominant bands by ~1.1 eV, leading to slow nonradiative internal conversion from Cu band to C and O bands. This is observed in the results from the combination of OTA and XTA kinetics that show a persistent ESA feature which closely matches the lifetime of the XTA signal, indicating that the Cu^{2+} ions are reduced for longer than 10 ns. Conversely, the GSB feature from OTA recovers on a timescale very similar to the THz attenuation from OPTP which suggests that photoexcitation generates a mobile hole. These differences between the longer lived XTA and OTA features and the shorter lived OPTP and OTA features are pronounced in Cu-HHTP relative to Cu/Zn-HHTP and Zn-HHTP because the Cu bands are flat and energetically isolated, trapping electrons and preventing electron/hole recombination. Looking at the Zn-HHTP band structures (Figure S11), we do not observe any similar Zn density of states due to the redox inactivity of Zn, which prevents electron trapping leading to strongly bound HHTP localized excitons resulting in marginal THz attenuation, and lower photoconductivity. Furthermore, the energy gap law explains why the initial relaxation component from OTA is slower in Zn-HHTP than Cu-HHTP because of the larger gap between the HHTP localized bands in Zn-HHTP (~2.1 eV) than the HHTP and Cu localized bands in Cu-HHTP (~0.4 eV). These results well explain the much higher photoconductivity in Cu-HHTP compared to other MOF systems, which can be attributed to the presence of an effective hole transport pathway, facilitated by the strong π-π interaction between HHTP ligands. This is further supported by the direct comparison of photoconductivity between Cu-HHTP with Cu-THQ (THQ=tetra-hydroxybenzoquinone),[31] where the former exhibits a more than two orders of magnitude increase in photoconductivity (Table S3) compared to the latter which was believed to possess a negligible hole transport pathway.

Conclusion

In summary, we have examined the photoconductivity in the conductive 2D M-HHTP (M=Cu and/or Zn) MOF using the non-contact photoconductivity measurements, namely OPTP. These findings reveal the remarkable optical and electrical properties of M-HHTP, e.g., Cu-HHTP and Zn-HHTP. The photoconductivity of Cu-HHTP is 65.5 $S \cdot m^{-1}$, which is higher than previously reported conductivity results, and the best point of reference currently available for spectroscopic conductivity results. With the aid of OTA and XTA spectra and TDDFT, we reveal that the ultrafast charge transport dynamics in Cu-HHTP is attributed to the photoexcited hole states through the interlayer π-π interaction between HHTP ligands. More significantly, it is the first time to demonstrate the quantitative evaluation of the photoconductivity mechanism in 2D MOFs, paving the way for the development of novel photoconductive porous 2D-MOFs in electronics and photoelectronic applications as well as their mechanism of study.

Supporting Information

Supporting Information (PDF). Including EDX spectrum of M-HHTP; The fitting parameters of XAS data. EXAFS spectra in k-space; The data of XTA. DFT calculation detail procedure and parameters.

Acknowledgements

This work is supported by the U.S. Department of Energy, Office of Science, Office of Basic Energy Sciences, under Award No.

DE-SC0024049. Use of the Advanced Photon Source in Argonne National Laboratory is supported by the U.S. Department of Energy, Office of Science, Office of Basic Energy Sciences, under award no. DE-AC02-06CH11357. The research at Yale was supported by the National Science Foundation (NSF) under grant no. CHE-1954453.

Keywords: 2D-MOF • photoconductivity • hole transport • terahertz spectroscopy • DFT calculation

[1] aH. Li, M. Eddaoudi, M. O'Keeffe, O. M. Yaghi, *Nature* **1999**, *402*, 276-279; bL. E. Kreno, K. Leong, O. K. Farha, M. Allendorf, R. P. Van Duyne, J. T. Hupp, *Chem. Rev.* **2012**, *112*, 1105-1125; cC.-D. Wu, A. Hu, L. Zhang, W. Lin, *J. Am. Chem. Soc.* **2005**, *127*, 8940-8941; dB. Li, H.-M. Wen, W. Zhou, B. Chen, *J. Phy. Chem. Lett.* **2014**, *5*, 3468-3479; eW. Cai, J. Wang, C. Chu, W. Chen, C. Wu, G. Liu, *Adv. Sci.* **2019**, *6*, 1801526.

[2] aA. A. Talin, A. Centrone, A. C. Ford, M. E. Foster, V. Stavila, P. Haney, R. A. Kinney, V. Szalai, F. El Gabaly, H. P. Yoon, F. Léonard, M. D. Allendorf, *Science* **2014**, *343*, 66-69; bL. Sun, M. G. Campbell, M. Dincă, *Angew. Chem. Int. Ed.* **2016**, *55*, 3566-3579.

[3] aL. E. Darago, M. L. Aubrey, C. J. Yu, M. I. Gonzalez, J. R. Long, *J. Am. Chem. Soc.* **2015**, *137*, 15703-15711; bT. Kambe, R. Sakamoto, K. Hoshiko, K. Takada, M. Miyachi, J.-H. Ryu, S. Sasaki, J. Kim, K. Nakazato, M. Takata, H. Nishihara, *J. Am. Chem. Soc.* **2013**, *135*, 2462-2465; cD. Sheberla, J. C. Bachman, J. S. Elias, C.-J. Sun, Y. Shao-Horn, M. Dincă, *Nat. Mater.* **2017**, *16*, 220-224; dD. Sheberla, L. Sun, M. A. Blood-Forsythe, S. Er, C. R. Wade, C. K. Brozek, A. Aspuru-Guzik, M. Dincă, *J. Am. Chem. Soc.* **2014**, *136*, 8859-8862; eI. Stassen, N. C. Burtch, A. A. Talin, P. Falcaro, M. D. Allendorf, R. Ameloot, *Chem. Soc. Rev.* **2017**, *46*, 3853-3853; fB. Pattengale, S. Ostresh, C. A. Schmuttenmaer, J. Neu, *Chem. Rev.* **2021**, *122*, 132-166; gZ. Zhuang, D. Liu, *Nano-Micro. Lett.* **2020**, *12*, 132; hL. S. Xie, G. Skorupskii, M. Dincă, *Chem. Rev.* **2020**, *120*, 8536-8580; iK. Chen, C. A. Downes, J. D. Goodpaster, S. C. Marinescu, *Inorg. Chem.* **2021**, *60*, 11923-11931; jG. Skorupskii, B. A. Trump, T. W. Kasel, C. M. Brown, C. H. Hendon, M. Dincă, *Nat. Chem.* **2020**, *12*, 131-136; kG. Skorupskii, M. Dincă, *J. Am. Chem. Soc.* **2020**, *142*, 6920-6924; lJ. Nyakuchena, S. Ostresh, D. Streater, B. Pattengale, J. Neu, C. Fiankor, W. Hu, E. D. Kinigstein, J. Zhang, X. Zhang, C. A. Schmuttenmaer, J. Huang, *J. Am. Chem. Soc.* **2020**, *142*, 21050-21058.

[4] D. W. Feng, T. Lei, M. R. Lukatskaya, J. Park, Z. H. Huang, M. Lee, L. Shaw, S. C. Chen, A. A. Yakovenko, A. Kulkarni, J. P. Xiao, K. Fredrickson, J. B. Tok, X. D. Zou, Y. Cui, Z. A. Bao, *Nature Energy* **2018**, *3*, 30-36.

[5] aK. Wada, K. Sakaushi, S. Sasaki, H. Nishihara, *Angew. Chem. Int. Ed.* **2018**, *57*, 8886-8890; bS. Gu, Z. Bai, S. Majumder, B. Huang, G. Chen, *J. Power Sources* **2019**, *429*, 22-29.

[6] K. J. Erickson, F. Leonard, V. Stavila, M. E. Foster, C. D. Spataru, R. E. Jones, B. M. Foley, P. E. Hopkins, M. D. Allendorf, A. A. Talin, *Adv. Mater.* **2015**, *27*, 3453-3459.

[7] aM. K. Smith, K. A. Mirica, *J. Am. Chem. Soc.* **2017**, *139*, 16759-16767; bM. G. Campbell, D. Sheberla, S. F. Liu, T. M. Swager, M. Dincă, *Angew. Chem. Int. Ed.* **2015**, *54*, 4349-4352; cY. Liu, Y. Wei, M. Liu, Y. Bai, G. Liu, X. Wang, S. Shang, W. Gao, C. Du, J. Chen, Y. Liu, *Angew. Chem. Int. Ed.* **2021**, *60*, 17440-17445; dX. Song, X. Wang, Y. Li, C. Zheng, B. Zhang, C.-a. Di, F. Li, C. Jin, W. Mi, L. Chen, W. Hu, *Angew. Chem. Int. Ed.* **2020**, *59*, 1118-1123; eV. Rubio-Giménez, N. Almora-Barrios, G. Escorcia-Ariza, M. Galbiati, M. Sessolo, S. Tatay, C. Martí-Gastaldo, *Angew. Chem. Int. Ed.* **2018**, *57*, 15086-15090; fM.-S. Yao, X.-J. Lv, Z.-H. Fu, W.-H. Li, W.-H. Deng, G.-D. Wu, G. Xu, *Angew. Chem. Int. Ed.* **2017**, *56*, 16510-16514.

[8] aE. M. Miner, T. Fukushima, D. Sheberla, L. Sun, Y. Surendranath, M. Dincă, *Nat. Commum.* **2016**, *7*, 10942; bE. M. Miner, S. Gul, N. D. Ricke, E. Pastor, J. Yano, V. K. Yachandra, T. Van Voorhis, M. Dincă, *Acs Catal* **2017**, *7*, 7726-7731; cE. M. Miner, L. Wang, M. Dincă, *Chem. Sci.* **2018**, *9*, 6286-6291; dA. J. Clough, J. W. Yoo, M. H. Mecklenburg, S. C. Marinescu, *J. Am. Chem. Soc.* **2015**, *137*, 118-121.

[9] aZ. Zhao, J. Bian, L. Zhao, H. Wu, S. Xu, L. Sun, Z. Li, Z. Zhang, L. Jing, *Chin. J. Catal.* **2022**, *43*, 1331-1340; bS. Zhao, J. Xu, M. Mao, L. Li, X. Li, *J. Colloid Interface Sci.* **2021**, *583*, 435-447; cJ. Li, X. Li, G. Wu, J. Guo, X. Yin, M. Mu, *J. Environ. Chem. Eng.* **2021**, *9*, 106723; dJ. Qin, B. Liu, K.-H. Lam, S. Song, X. Li, X. Hu, *ACS Sustainable Chem. Eng.* **2020**, *8*, 17791-17799.

[10] E. Castaldelli, K. D. G. Imalka Jayawardena, D. C. Cox, G. J. Clarkson, R. I. Walton, L. Le-Quang, J. Chauvin, S. R. P. Silva, G. J.-F. Demets, *Nat. Commum.* **2017**, *8*, 2139.

[11] aB. Pattengale, J. Neu, S. Ostresh, G. Hu, J. A. Spies, R. Okabe, G. W. Brudvig, C. A. Schmuttenmaer, *J. Am. Chem. Soc.* **2019**, *141*, 9793-9797; bB. Pattengale, J. G. Freeze, M. J. Guberman-Pfeffer, R. Okabe, S. Ostresh, S. Chaudhuri, V. S. Batista, C. A. Schmuttenmaer, *Chem. Sci.* **2020**, *11*, 9593-9603.

[12] Y. Misumi, A. Yamaguchi, Z. Zhang, T. Matsushita, N. Wada, M. Tsuchiizu, K. Awaga, *J. Am. Chem. Soc.* **2020**, *142*, 16513-16517.

[13] R. W. Day, D. K. Bediako, M. Rezaee, L. R. Parent, G. Skorupskii, M. Q. Arguilla, C. H. Hendon, I. Stassen, N. C. Gianneschi, P. Kim, M. Dincă, *ACS Cent. Sci.* **2019**, *5*, 1959-1964.

[14] X. Li, J. Yu, D. J. Gosztola, H. C. Fry, P. Deria, *J. Am. Chem. Soc.* **2019**, *141*, 16849-16857.

Entry for the Table of Contents

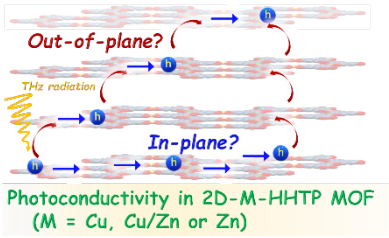

We report the mechanisms of photoinduced charge transport and electron dynamics in the conductive 2D MOFs and their correlation with photoconductivity using multiple spectroscopy techniques. We identify the through-space hole transport mechanism through the interlayer sheet π-π interaction, where the photoinduced hole state resides in the HHTP ligand and the electronic state is localized at the metal center.